




STRUCTURAL CHARACTERIZATION AND THERMAL DECOMPOSITION OF LIME BINDERS ALLOW ACCURATE RADIOCARBON AGE DETERMINATIONS OF AERIAL LIME PLASTER

Michael B Toffolo^{1*}  • Lior Regev²  • Eugenia Mintz² • Ifat Kaplan-Ashiri³ • Francesco Berna⁴ • Stéphan Dubernet¹  • Xin Yan² • Johanna Regev² • Elisabetta Boaretto²

¹Institut de Recherche sur les Archéomatériaux-Centre de Recherche en Physique Appliquée à l'Archéologie (IRAMAT-CRP2A), UMR 5060 CNRS, Université Bordeaux Montaigne, 8 Esplanade des Antilles, Pessac 33607, France

²D-REAMS Radiocarbon Dating Laboratory, Weizmann Institute of Science, 234 Herzl Street, Rehovot 7610001, Israel

³Department of Chemical Research Support, Weizmann Institute of Science, 234 Herzl Street, Rehovot 7610001, Israel

⁴Department of Archaeology, Simon Fraser University, 8888 University Drive, Burnaby, BC V5A 1S6, Canada

ABSTRACT. Radiocarbon (¹⁴C) dating of anthropogenic carbonates (CaCO₃) such as ash, lime plaster and lime mortar, has proven a difficult task due to the occurrence of a number of contaminants embedded within the CaCO₃ pyrogenic binder. These include ¹⁴C-free geologic components and/or secondary phases bearing an unknown amount of ¹⁴C, and thus the alteration of the original pyrogenic isotopic signature of the material results in major age offsets when carbon recovery is performed through acid hydrolysis. Here we present a characterization/quantification approach to anthropogenic carbonates that includes Fourier transform infrared spectroscopy (FTIR), X-ray diffraction, thin section petrography, thermogravimetric analysis and scanning electron microscopy coupled with high-resolution cathodoluminescence, with which we identified the pyrogenic CaCO₃ fraction in an aerial lime plaster and two hydraulic mortars. The preserved pyrogenic component was then isolated by density separation and its purity checked again using FTIR. Carbon was recovered through thermal decomposition in vacuum. The resulting ¹⁴C age matches the expected age of the lime plaster, whereas hydraulic mortars are slightly offset due to the carbonation of calcium hydroxide lumps. This approach highlights the importance of a dedicated characterization strategy prior to dating and may be applied to aerial lime plasters to obtain accurate ages.

KEYWORDS: calcite, carbonate, hydraulic, lime mortar, lime plaster.

INTRODUCTION

Anthropogenic carbonates, such as ash, lime plaster and lime mortar, are human-made materials composed of calcium carbonate (CaCO₃) that are produced through pyrotechnological processes (Weiner 2010; Artioli 2010). These involve the thermal decomposition of a CaCO₃ substrate (e.g. limestone, chalk, dolomite, calcite ash pseudomorphs derived from calcium oxalates in plants) at temperatures above 750°C to produce quicklime, CaO, which is slaked with water to obtain hydrated lime, Ca(OH)₂. In ash, this happens by reaction with humidity in air. A silicate (e.g. quartz sand) or carbonate (e.g. limestone pebbles) aggregate may be added to Ca(OH)₂ to increase volume and enhance the mechanical stability and durability of the final product. Hydrated lime turns back to CaCO₃, usually in the form of calcite, upon incorporation of carbon dioxide (CO₂) from air and evaporation of water (Boynton 1980; Xu et al. 2015, 2016). Atmospheric CO₂ contains radiocarbon (¹⁴C), which in principle can be extracted from pyrogenic CaCO₃ and measured to obtain age determinations representative of the time of setting of the plaster/mortar/high-temperature ash (e.g. Labeyrie and Delibrias 1964; Boaretto and Poduska 2013). Considering that anthropogenic carbonates have been used by humans since prehistoric times (e.g. Kingery et al. 1988; Berna et al. 2012), the ability to date the mineral fraction in the absence of organics would considerably expand the range of materials available for ¹⁴C dating at archaeological sites. In particular, the

*Corresponding author. Email: michael.toffolo@u-bordeaux-montaigne.fr.

chronological study of decorative (e.g. plastered walls) and functional (e.g. binder between cobbles) mortars in ancient architectures would greatly benefit from the possibility of obtaining accurate dates. However, ^{14}C dating of anthropogenic carbonates has so far proven a difficult and often unproductive task due to the occurrence of a number of contaminants embedded within the pyrogenic CaCO_3 fraction (Koumouzelis et al. 2001; Regev et al. 2011; Hajdas et al. 2017; Hayen et al. 2017).

Early attempts to date medieval mortars characterized by a silicate aggregate, and based on CO_2 recovery through thermal decomposition of the CaCO_3 binder, were successful (Labeyrie and Delibrias 1964; Delibrias and Labeyrie 1965). Soon after, thermal decomposition was replaced by acid hydrolysis, but results proved impossible to replicate with samples containing a carbonate aggregate (Stuiver and Smith 1965; Baxter and Walton 1970). The presence of ^{14}C -free geogenic carbonates embedded in the lime binder produced older ages, although it was noted that the first CO_2 fraction evolved during hydrolysis yields more accurate ages, as it should represent the more soluble pyrogenic carbonates. This problem led to the introduction of the mechanical separation of binder and aggregate prior to CO_2 recovery. Results thus obtained produced more accurate age determinations, which however still showed significant offsets compared to the expected age, presumably due to residual geogenic or secondary carbonates (Folk and Valastro 1976). The latter are a product of the dissolution of pyrogenic CaCO_3 exposed to carbonic acid from groundwater, and may be contaminated by younger carbon (Boaretto and Poduska 2013). As a consequence, ^{14}C dating of mortars never became a routine laboratory procedure and only a few applications were reported in the 1980s (e.g. Zouridakis et al. 1987). This situation persisted until the late 1990s, when CO_2 recovery by acid hydrolysis was resumed and improved by sample prescreening based on cathodoluminescence and sequential dissolution of the lime binder, and the introduction of accelerator mass spectrometry (AMS) allowed the measurement of smaller carbon aliquots (e.g. Heinemeier et al. 1997; Lindroos et al. 2007). This approach rests on the assumption that pyrogenic CaCO_3 dissolves immediately after secondary carbonates (if present) and before geogenic aggregates. By collecting CO_2 at different intervals after the beginning of the hydrolysis reaction it is possible to isolate the CO_2 aliquot that is supposed to represent the age of the pyrogenic binder, although no specific time intervals have been suggested and the correlation between origin of the evolved CO_2 and relative ^{14}C age is based on expected age as indicated by archaeological assessments or other independent age controls. This degree of uncertainty regarding the nature of the dissolved fraction (e.g. secondary/pyrogenic/geogenic carbonates, hydraulic carbonates, or a mixture thereof) required the introduction of guiding criteria in the interpretation of results (Heinemeier et al. 2010). Despite the use of criteria, this method produced somewhat contrasting results, as ^{14}C dates are in some cases affected by significant deviations from the true age of the archaeological sample, especially in the case of hydraulic mortars (Murakami et al. 2013; Ringbom et al. 2014; Ponce-Antón et al. 2018; Michalska 2019). Improvements in the purification of lime binders yielded more accurate and promising results (e.g. Addis et al. 2016; Addis et al. 2019), although a recent international intercomparison exercise confirmed that at present there is no methodology able to provide accurate and reproducible ^{14}C dates for any type of mortar (Hajdas et al. 2017; Hayen et al. 2017).

The discrepancies between expected age and ^{14}C measurements are of difficult explanation, but are mainly caused by the fact that the particle size fractions selected for hydrolysis are comprised of a mixture of different types of carbonates, and hydrolysis itself allows little

control over what is actually dissolved at any given time during the reaction. In other words, the key issue is to identify and isolate one dateable fraction that is *a priori* known to represent the time of formation of the lime binder. Recently, Toffolo et al. (2017a) showed that it is possible to obtain accurate ^{14}C dates from pyrogenic aragonite in archaeological ash deposits. Aragonite is one of the metastable polymorphs of CaCO_3 , and may nucleate as needle-shaped crystals upon carbonation of CaO and $\text{Ca}(\text{OH})_2$ in lime plaster and high-temperature ash, thus representing the time of formation of the combustion feature/artifact (Toffolo and Boaretto 2014). These needles might be related to the “calcium carbonate needles” targeted by Labeyrie and Delibrias (1964) in their pioneering study. Pyrogenic aragonite was isolated from other contaminants by density and decomposed at 550°C to evolve CO_2 , which matched the expected age of the ash deposit based on ^{14}C dating of charred seeds recovered from the same sedimentary context (Toffolo et al. 2017a). Since pyrogenic aragonite does not always nucleate in anthropogenic carbonates, we decided to apply the same method to pyrogenic calcite, which is the most common CaCO_3 polymorph in lime plaster/mortar. Here we show that by carefully characterizing and quantifying the phases occurring in archaeological samples, we were able to identify the original pyrogenic calcite fraction. This procedure was applied to an aerial lime plaster from a Byzantine church at Shivta and two hydraulic mortars from Wilson’s Arch in Jerusalem (both sites are located in Israel). The pristine carbonate was then isolated by density and decomposed at 500°C to recover CO_2 . The carbon aliquot obtained for Shivta yielded a ^{14}C date that matches the expected age of the sample, whereas the purified fractions of Wilson’s Arch mortars are offset due to the carbonation of $\text{Ca}(\text{OH})_2$ aggregates (lime lumps). These results show that thermal decomposition of pyrogenic calcite can be used to obtain accurate ^{14}C dates from anthropogenic carbonates, and that hydraulic contaminants can be removed. In addition, serious concerns are raised over the carbon contribution from lime lumps.

MATERIALS AND METHODS

Archaeological Contexts and Materials

Shivta (henceforth SHV) is located in the Negev Desert, Israel. This settlement prospered during the Roman-Byzantine period (1st–7th c. CE) and was abandoned after the Early Islamic period in the 9th c. CE. SHV was first excavated in the 1930s (Avni 2014), and new excavations have been carried out in 2015–2016. The plaster sample was collected from the wall of an extension chamber in the Northern Church of the Byzantine period (6th–7th c. CE), where it provided a finishing coat to the structure (Figure 1) (Tepper et al. 2018).

The site of Wilson’s Arch (henceforth KW) is located in Jerusalem’s Old City. In the past, the arch itself led to the Temple Mount. Excavations beneath Wilson’s Arch were conducted between 2015 and 2018 by the Israel Antiquities Authority over an area of 200 m^2 and to a depth of 10 m (Uziel et al. 2019). Two coating mortars (KW4213 and KW4215) were collected from two superimposed pools of presumably medieval or post-medieval age (Figure 1). Both samples contain a preserved grass temper, which was used to obtain an independent age control.

Fourier Transform Infrared Spectroscopy (FTIR)

Different portions of the SHV lime plaster and KW lime mortars were sampled to determine their composition. A few milligrams of each binder were homogenized and powdered in an agate mortar and pestle. About 0.1 mg were left in the mortar and mixed with



Figure 1 Materials analyzed in this study. Top: chunks of mortars selected for characterization and dating. Bottom: scans of thin sections (long side of each slide: 5 cm).

approximately 0.5 mg of KBr (FTIR grade, Sigma-Aldrich) and pressed into a 7-mm pellet using a hand press (PIKE Technologies). Infrared spectra were obtained at 4 cm^{-1} resolution in 32 scans within the $4000\text{--}400\text{ cm}^{-1}$ spectral range using a Bruker Alpha spectrometer or a Thermo Fisher Scientific Nicolet iS5 spectrometer. Phase identification was performed using OMNIC v. 9, standard literature (Farmer 1974; van der Marel and Beutelspacher 1976) and the reference collection of FTIR spectra of standard materials provided by the Kimmel Center for Archaeological Science, Weizmann Institute of Science (<http://www.weizmann.ac.il/kimmel-arch/infrared-spectra-library>). The infrared grinding curve method of Regev et al. (2010), based on a theoretical study by Poduska et al. (2011), was used to determine the degree of atomic order of calcite crystals and thus the state of preservation of the pyrogenic carbonate fraction.

X-Ray Diffraction (XRD)

Samples were characterized with XRD to identify contaminants not readily visible with FTIR, such as layered double hydroxides (LDH) and other phases that typically form during

hydraulic reactions and may contain younger carbon (Artioli et al. 2017). Powdered aliquots of the SHV and KW samples were analyzed with a 300 mm radius Bruker D8 Advance goniometer configured in Bragg-Brentano mode, under the incident X-ray doublet $\text{CuK}\alpha$ combined with a 2.6° (180 px) linear Bruker LynxEye detector. The minor phases detection with good statistics was reached by acquisition for 550 s each 0.01° points in the range 5–60° 2 θ . Sample holders in PolyMethyl MethAcrylate and Si oriented of respective diameters 25 and 20 mm were used depending on the amount of material (0.5 and 0.16 cm³). The contributions of the continuous background and of the $\text{CuK}\alpha_2$ were removed by Bruker DIFFRAC.EVA v.4.2 software. The mineral identification and the semi-quantitative analysis were performed using the ICDD PDF2-2004 database patterns.

Thin Section Petrography

The spatial distribution and relations of different mortar components were observed at the microscale using thin sections. Small chunks of each sample were embedded in vacuum in a mixture of epoxy resin and hardener (10:3). Solid blocks were cut using a rock saw to obtain 20 × 35 mm chips, which were mounted onto glass slides and polished to 30 μm in thickness. Thin sections were analyzed using a Leica DM2500 P petrographic microscope at different magnifications (25×, 50×, 100×, 200×, 400×).

Fourier Transform Infrared Micro-Spectroscopy (μFTIR)

Thin sections of the SHV plaster and KW4213 mortar were analyzed with μFTIR to determine the spatial distribution of different phases, and in particular of CaCO_3 crystals characterized by different degrees of atomic order. Analyses were performed using a Thermo Fisher Scientific Nicolet iN10 MX FTIR image microscope in transmission and reflection mode. Spectra were collected with 50 × 50 μm aperture at 8 cm^{-1} resolution in 8 or 16 scans within the 4000–650 cm^{-1} spectral range. Areas of variable size within the lime binder were mapped at 50 μm spatial resolution. Phase identification and chemical map generation were performed with OMNIC Picta™ using a reference spectral library containing FTIR spectra of experimental pyrogenic calcite, sparitic calcite, micritic calcite, dolomite, aragonite, quartz, and epoxy resin used for the preparation of the thin sections. The abovementioned carbonate phases are best distinguished based on peak location and on the width of the ν_3 (CO_3) band in the case of calcites formed by different mechanisms (Poduska et al. 2012).

Density Separation

Pyrogenic carbonates (i.e. calcite and aragonite) are characterized by lower specific gravity compared to their geogenic counterparts (e.g. Moropoulou et al. 1995; Toffolo et al. 2017a). Thus, we exploited density to isolate the pyrogenic, light carbonates from the geogenic, heavy carbonates. To do so, we modified the procedure of Toffolo et al. (2017a) for pyrogenic aragonite. The SHV plaster and KW mortars were powdered with an agate mortar and pestle and sieved to collect the fraction smaller than 63–50 μm , of which 100-mg aliquots were placed inside 15-mL plastic tubes; up to 8 tubes were used and thus up to 800 mg of sample for each round of separation. Each aliquot was mixed with 300 μL of 1M sodium phosphate dibasic (Na_2HPO_4 ; Sigma-Aldrich) in deionized water, and the resulting solution was vortexed a few seconds until complete mixing. After, 4 mL of sodium polytungstate (SPT; $3\text{Na}_2\text{WO}_4 \cdot 9\text{WO}_3 \cdot \text{H}_2\text{O}$) in deionized water at 2.6 g/mL density were added and the resulting solution was vortexed a few seconds. We used SPT poor in carbon (~100 ppm) by

TC-Tungsten Compounds GmbH (Grub am Forst, Germany) to avoid contamination. Mixing SPT with the sodium phosphate buffer lowered density to 2.5 g/mL. By doing so, it is possible to avoid geogenic/biogenic calcite (2.71 g/mL), dolomite (2.86 g/mL), and geogenic/biogenic aragonite (2.94 g/mL) (Lippmann 1973). In addition, the sodium phosphate buffer keeps pH around 8, thus preserving CaCO₃ crystals from dissolution in an acidic heavy liquid (the pH of SPT at high density is ~4). Tubes were sonicated 10 min and centrifuged 20 min at 4000 rpm. Light fractions were pipetted out and transferred to 2-mL plastic tubes. The remaining solution was discarded and the heavy fractions were pipetted out from the bottom of the tube by rinsing with deionized water and transferred to 2-mL plastic tubes. Light and heavy fractions were rinsed at least 4 times with deionized water until pH 7 was reached. In case of low yield, the entire separation procedure may be repeated. Finally, light fractions were rinsed with 1 mL of 0.1M NaOH for 5 min to remove humic acids. In the specific case, solutions were transparent. Earlier tests by Toffolo et al. (2017a) showed that there is no uptake of atmospheric CO₂ in such conditions. Samples were rinsed with deionized water until pH 7 was reached and dried in an oven at 60°C.

Cathodoluminescence by Scanning Electron Microscopy (SEM-CL)

Samples were analyzed with SEM-CL to determine the presence of geogenic carbonate contaminants in the purified fractions. When observed with an optical microscope, geogenic carbonates are characterized by orange-red luminescence caused by the substitution of Ca²⁺ with Mn²⁺ in the CaCO₃ crystal lattice, whereas the pyrogenic lime binder emits dark-red to brown luminescence (Machel 2000; Lindroos et al. 2007). This different color is caused by the overlap of two emissions, one in the orange caused by Mn²⁺ and one in the blue caused by lattice distortions (Toffolo et al. 2019b). Small aliquots (ca. 10 mg) of each purified fraction were pressed into a 3-mm pellet using a hand press (PIKE Technologies). Pellets were mounted on SEM stubs using carbon tape and were coated with a layer of carbon 7–8 nm thick using a sputter coater (Safematic CCU-010). To collect SEM-CL spectra we used a Gatan MonoCL Elite system equipped with a retractable diamond-turned mirror. The collected light first was imaged in panchromatic mode using a high-sensitivity photomultiplier tube with a spectral range of 160–930 nm. The collected light was directed to a monochromator and a charge-coupled device for parallel spectroscopy. The spectral range was set to 300–800 nm with a band pass of 20 nm by choosing the 150 lines/mm grating centered on 550 nm and 1 mm entrance slit. The CL system is installed on a Zeiss Gemini SEM 500, a high-resolution SEM equipped with a two-modes field emission gun. CL measurements were performed at 20 kV with an aperture of 20 µm in analytical gun mode. CL was collected in spectrum imaging (SI) mode, with 4.3 µm pixel size and 0.5 s exposure time per pixel. The simultaneous SEM images were collected using the SE2 detector (Everhardt-Thornely detector). For each sample the SI was collected at several different regions of interest (ROI), then the spectra were analyzed by Gaussian fitting in order to extract the emission wavelength, the intensity and the full width at half maximum (FWHM) of the different bands.

Thermogravimetric Analysis (TGA)

TGA was performed to determine the temperature of decomposition of different phases in the purified fractions and thus tune temperature steps during CO₂ recovery. It is known that pyrogenic CaCO₃ loses carbonate groups at lower temperature compared to its geogenic counterpart, and thus CO₂ from pyrogenic CaCO₃ can be collected separately (e.g. Moropoulou

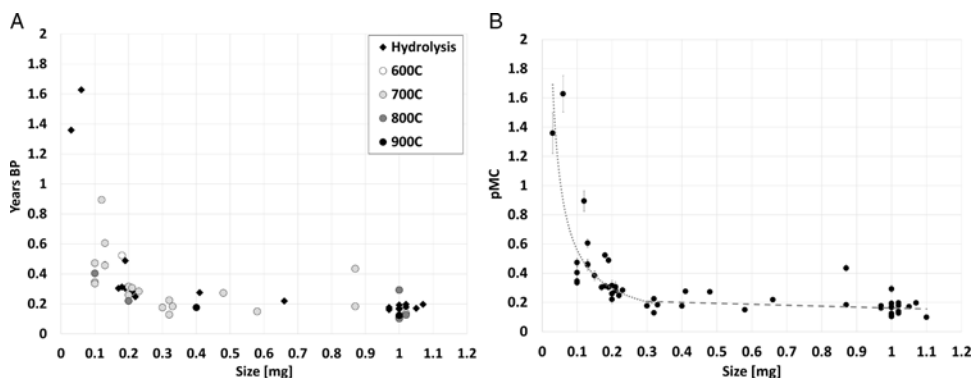


Figure 2 Plots showing the backgrounds used for thermal decomposition at different temperatures. A: results shown in years BP. B: results shown in pMC.

et al. 1995; Anastasiou et al. 2006; Toffolo et al. 2017a). Small aliquots (ca. 10 mg) of each purified fraction were placed in an alumina crucible and heated in nitrogen atmosphere from room temperature to 900°C, at a heating rate of 10°C per minute, using an SDT Q600 V8.3 Build 101 thermal analyzer. For KW4213, we added a 1-hr step at 500°C.

Radiocarbon Dating

As shown by Toffolo et al. (2017a), purified samples may contain ~1% or more of geogenic contaminants presumably due to the presence of intergrown minerals characterized by a composite specific gravity, which falls within the range of the light fraction. The same study showed that this is the factor that causes CaCO₃ hydrolysis in phosphoric acid to produce ¹⁴C ages older than expected. By using thermogravimetric analysis, Toffolo et al. (2017a) also showed that pyrogenic carbonates decompose and release CO₂ at lower temperature compared to their geogenic equivalent, usually in the range 500–550°C. The relative carbon aliquots produced accurate age determinations. Therefore, we followed the same procedure and placed at least 400 mg of purified fraction in a quartz ampule under vacuum, which was then heated to 500 and 700°C using an electric muffle oven. In the case of SHV, also the heavy fraction was measured, with an additional temperature step at 800°C. The CO₂ evolved up to 500°C was discarded in order to avoid contamination from residual organic phases and from reactive clay minerals and/or LDH that contain [CO₃]²⁻ moieties (e.g. Ishihara et al. 2013; Sahoo et al. 2014; Addis et al. 2016; Artioli et al. 2017; Addis et al. 2019). LDHs decompose to an amorphous state at temperatures under 500°C (e.g. Rey et al. 1992; Roelofs et al. 2002; Tian and Qinghai 2014). Each temperature step lasted 1 hr. The different CO₂ aliquots were converted to graphite for AMS following Yizhaq et al. (2005). AMS measurements were performed at the D-REAMS Laboratory, Weizmann Institute of Science (Regev et al. 2017). Measurements were repeated to ensure reproducibility, and for KW4213 the first temperature step was raised to 550°C in one case to observe possible contributions from secondary calcite. A marble sample from Ness Ziona (Israel) was used as background. As no CO₂ was emitted from the marble sample at 500 and 550°C, the CO₂ collected at 700 and 800°C was used as background. In case of small sample size (<0.5 mg), Oxalic Acid II samples of similar size were used for normalization. A total of 52 background (BGD) samples were prepared and measured during this study (Supplementary Table S1 and Figure 2). Although different sample preparation methods were used (acid hydrolysis and thermal decomposition to various temperatures), no difference was observed in the BGD levels

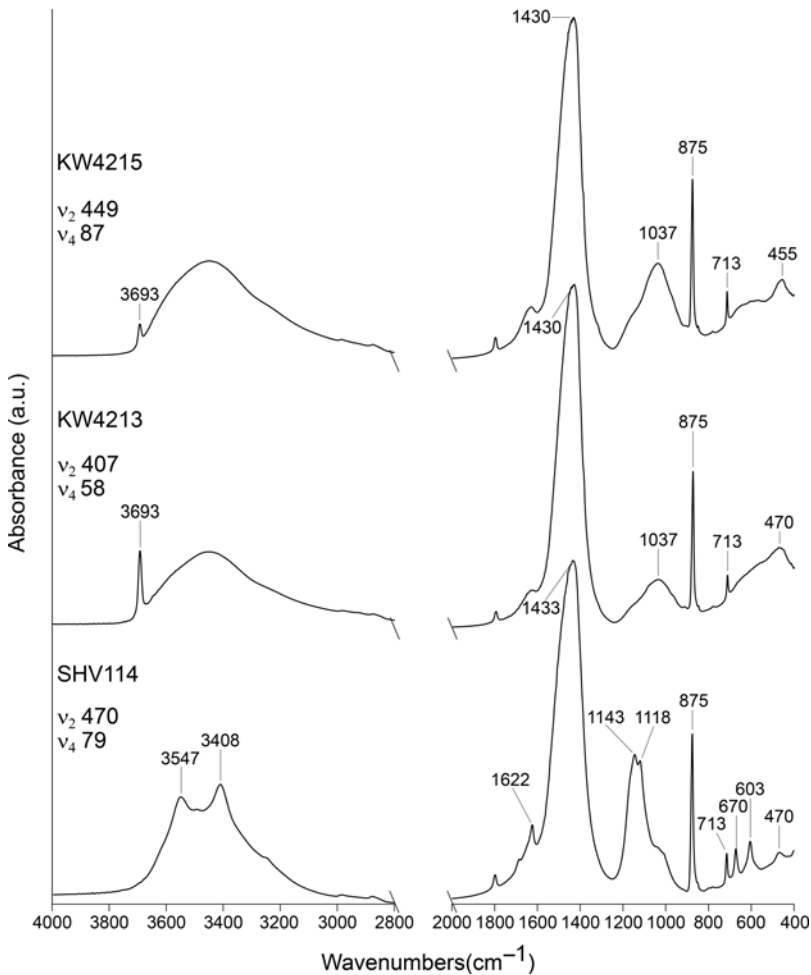


Figure 3 FTIR spectra of mortar samples, showing their ν_2 and ν_4 normalized heights.

of the different methods (Figure 2A). Therefore, two trendlines were calculated for the whole set of samples (Figure 2B). A linear trendline for samples ≥ 0.3 mg ($y = -0.0638x + 0.2255$, the sample at 0.87, 0.435 was excluded) and power function trendline for samples ≤ 0.35 mg ($y = 0.0675x^{-0.918}$). For each dated sample, the size-dependent BGD value was calculated based on the appropriate trendline. Linen and straw fibers embedded in the KW mortars were treated with 5% sodium chlorite (NaClO_2 ; Sigma-Aldrich) in deionized water at 80°C to recover cellulose, which was combusted to evolve CO_2 . The latter was converted to graphite following Yizhaq et al. (2005).

RESULTS AND DISCUSSION

Characterization

FTIR and XRD

Results of FTIR and XRD analyses are displayed in Figure 3 and Table 1, respectively. The SHV lime plaster is comprised mainly of calcite, with smaller amounts of quartz and gypsum.

Table 1 Sample composition based on semi-quantitative XRD analysis (in % of the crystalline phases; $\pm 5\%$).

| Sample | Calcite | Quartz | Gypsum | Hydrotalcite | Hydrocalumite | Pyroaurite-2H | Brucite | Portlandite | Ettringite | Diopside |
|--------|---------|--------|--------|--------------|---------------|---------------|---------|-------------|------------|----------|
| SHV114 | 81 | 11 | 8 | — | — | — | — | — | — | — |
| KW4213 | 40 | 2 | — | 5 | 12 | 7 | 9 | 20 | 5 | — |
| KW4215 | 64 | 10 | — | 4 | 4 | 12 | 3 | — | 2 | 1 |

The latter is likely a product of surface water evaporation in the arid environment of the Negev Desert. The KW lime mortars exhibit mainly calcite, variable amounts of portlandite, quartz, and LDH such as brucite and minerals belonging to the hydrotalcite supergroup, e.g. hydrocalumite and pyroaurite-2H (Mills et al. 2012). Remarkably, the KW mortars are characterized also by the presence of ettringite, a hydrous calcium aluminum sulfate. This mineral is one of the so-called intermediate alumina-ferric oxide-trisulfate (AFt) phases that form during the reaction between water and tricalcium silicate and calcium sulfate phases in Portland clinker, and that eventually turns into portlandite and amorphous calcium silicate hydrate (Artioli 2010; Pöllmann 2017). These results are confirmed by FTIR spectra, which exhibit absorption bands of calcite (1433, 875, 713 cm^{-1}), gypsum (3547, 3408, 1622, 1143, 1118, 670, 603 cm^{-1}) and quartz (470 cm^{-1}) for SHV, and calcite (1430, 875, 713 cm^{-1}), brucite (3693 cm^{-1}), quartz (470 cm^{-1}) and poorly ordered silicate phases (1037, 455 cm^{-1}) for KW. We should note that portlandite (calcium hydroxide; 3644 cm^{-1}) occurs only in specific aliquots of the KW mortars due to the presence of random lime lumps in the binder matrix. Following the infrared grinding curve method of Regev et al. (2010), we calculated the ν_2 and ν_4 normalized heights of calcite (Figure 3). Values fall above the experimental lime plaster curve for both samples (Regev et al. 2010: Figure 7), thus indicating the occurrence of the pristine pyrogenic fraction.

Thin Sections and μ FTIR

In thin section, SHV exhibits a fairly homogeneous groundmass of micritic calcite with embedded quartz grains, burnt and unheated limestone fragments (Figure 4a–b) and mollusk shells (Figure 4c). Gypsum occurs in pores close to the exposed surface of the plaster (Figure 4d), and one small lime lump was observed (Figure 4e–f). Instead, the KW mortars appear to be significantly more complex. Besides the micritic calcite groundmass with rare quartz grains, samples are characterized by fragments of burnt dolomite (Figure 5a), cellulose fibers from linen/straw (Figure 5b), and by a large number of ceramic fragments used as aggregate. The latter are surrounded by halos caused by the interaction between silicate and lime binder (Figure 5c–d). In crossed polarized light, these halos exhibit an isotropic groundmass, presumably rich in LDH, punctuated by calcite crystals. Carbonation fronts occur throughout the sample, together with lime lumps characterized by different degrees of carbonation (Figure 5e–f) (Karkanias 2007; Toffolo et al. 2017b). In KW4215, fibrous crystals of ettringite fill most of the pores (Figure 5g–h).

FTIR spectra collected from thin sections confirm that the micritic groundmass in both samples is mainly composed of poorly ordered calcite (Figures 6 and 7). More specifically, the position of the ν_3 absorption ranges between 1400–1410 cm^{-1} , which is consistent with experimental lime plaster (Poduska et al. 2012). Based on the width of the same peak, it is possible to observe locales showing different degrees of atomic order throughout the slides. μ FTIR shows that there are areas where pyrogenic calcite is slightly more ordered, thus indicating some degree of re-crystallization. However, we find that in the SHV114 chemical map the occurrence of slightly more ordered calcite (same degree of structural order as the micritic calcite reference) might be overestimated based on the overlap between the ν_3 peaks of reference experimental plaster and micritic calcite, which differ only with respect to the width of the shoulder at 1480 cm^{-1} . Furthermore, bulk FTIR analysis shows that SHV is extremely well preserved. Spectra acquired in transmission mode show the variability in concentration of portlandite and brucite throughout the KW4213 matrix, and thus the problematic nature of the sample with regard to the selection of suitable powders for dating (Supplementary Figure S1).

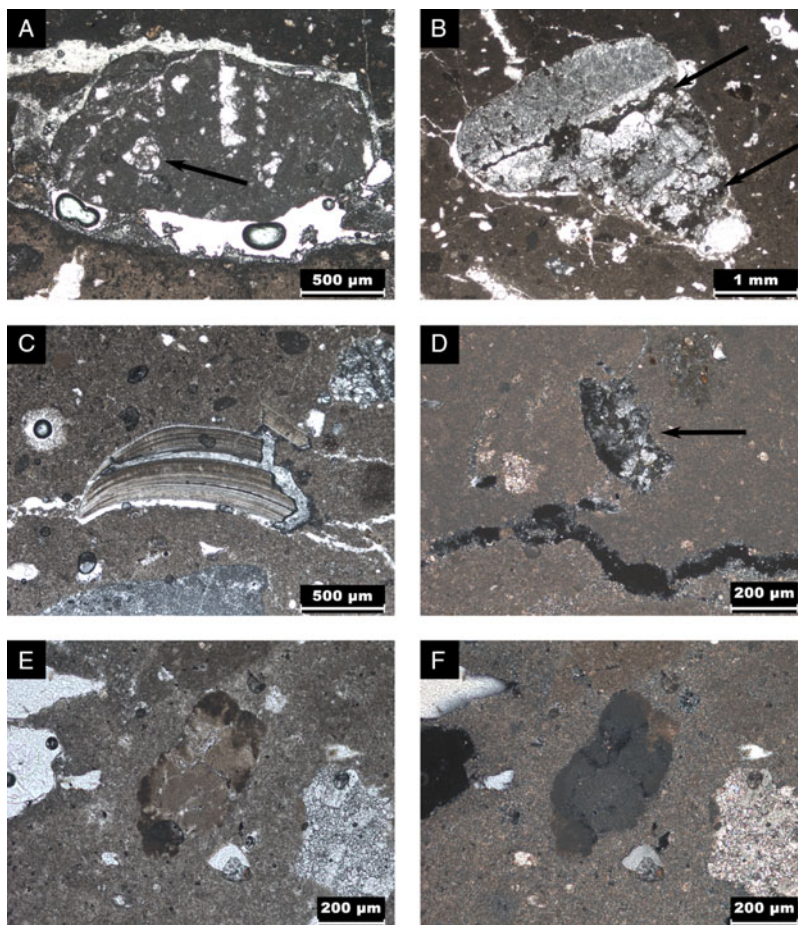


Figure 4 Photomicrographs of SHV114. A: burnt limestone fragment, note the microfossil (arrow). B: limestone fragment showing fissures filled with micritic calcite from the plaster binder (arrows). C: shell fragment (center of photo). D: gypsum intergrowth (arrow) in pore close to the exposed surface of the plaster, crossed polarized light. E: brown lime lump, center of image. F: same as previous in crossed polarized light, note the faint birefringence compared to the surrounding groundmass of micritic calcite. (Please see electronic version for color figures.)

Based on these results, we conclude that SHV was prepared using an aerial lime, whereas KW mortars underwent hydraulic reactions that caused the formation of LDH and ettringite (Artioli et al. 2017). In addition, the infrared absorption and XRD peaks of brucite lend support to the hypothesis that a certain proportion of dolomite was used as raw material for the production of quicklime; this is also indicated by the occurrence of burnt dolomite in thin section. The presence of a poorly ordered silicate phase similar to heated clay minerals as highlighted by FTIR, and the occurrence of ceramic fragments visible in thin section, make KW mortars equivalent to Roman *cocciopesto* in terms of composition, i.e. slaked lime mixed with a highly reactive ceramic phase (Artioli 2010; Hayen et al. 2017). Therefore, the reaction between $\text{Ca}(\text{OH})_2$ and ceramic fragments produced a mortar with hydraulic properties.

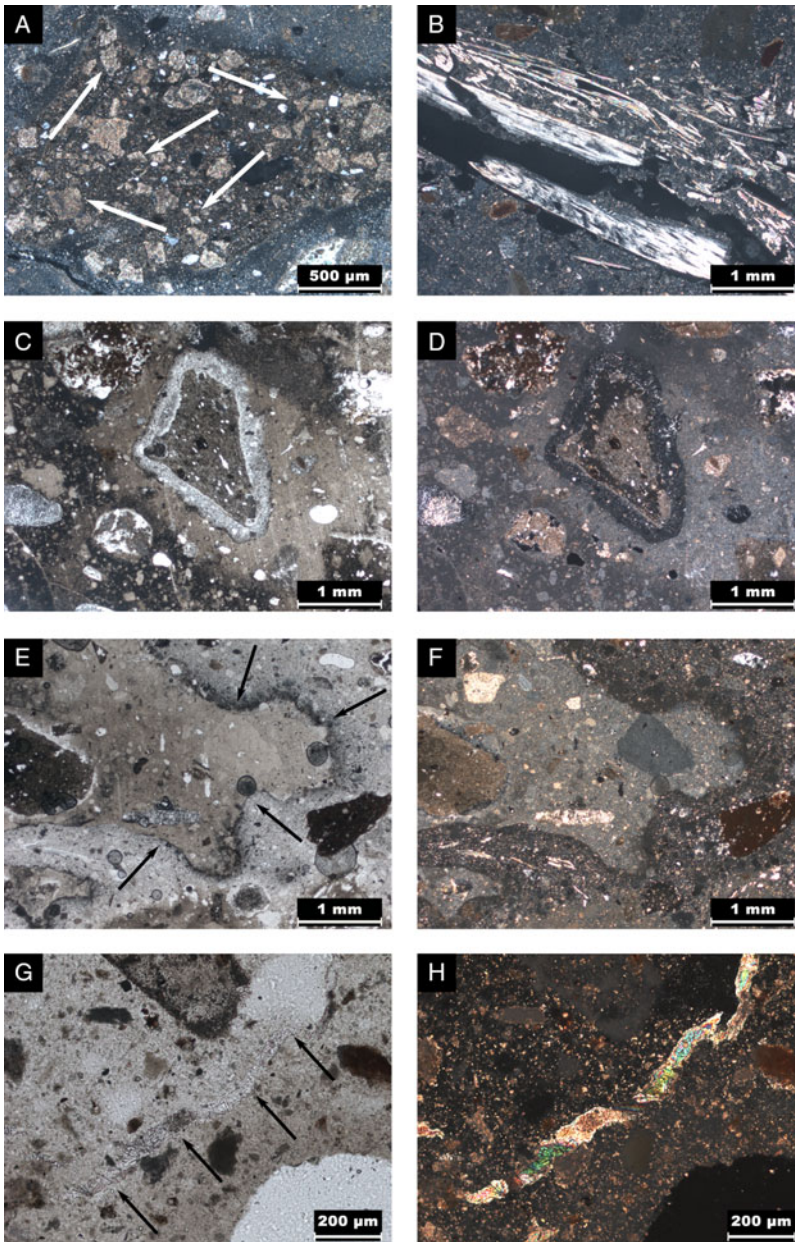


Figure 5 Photomicrographs of KW4213 and KW4215. A: burnt dolomite fragment in crossed polarized light, note the characteristic lozenge crystals (arrows) showing the birefringence of micritic calcite caused by exposure to elevated temperatures. B: cellulose fibers from the linen/straw temper, crossed polarized light. C: fragment of pottery embedded within the lime binder and surrounded by a halo of lighter groundmass. D: same as previous in crossed polarized light, note that the halo is mainly isotropic and punctuated by calcite crystals. E: carbonation front marked by the precipitation of Fe-Mn oxides (arrows). F: same as previous in crossed polarized light, note the isotropic groundmass to the right of the carbonation front. G: intergrowth of fibrous ettringite crystals (arrows). H: same as previous in crossed polarized light, note the high-order interference colors.

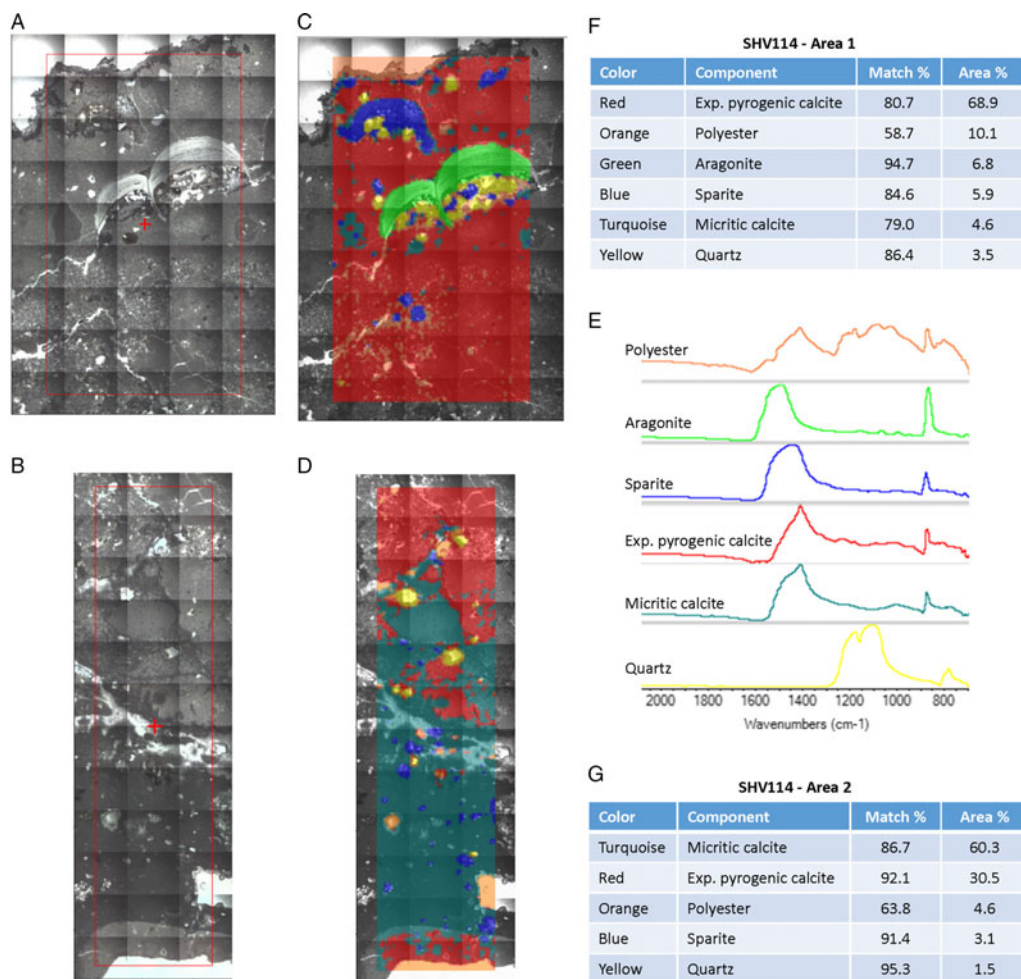


Figure 6 Micro-FTIR chemical maps of SHV114 showing areas characterized by different phases. A: video mosaic of Area 1 mapped in reflection mode. B: video mosaic of Area 2 mapped in reflection mode. C: color-coded chemical map of Area 1. D: color-coded chemical map of Area 2. E: reference FTIR spectra used to create the chemical maps of Area 1 and 2. F: quantitative analysis table from Area 1. Note that over 60% of the material analyzed appears to be composed of calcite with FTIR spectral characteristics similar to those of experimental pyrogenic calcite (i.e. experimental lime plaster). G: quantitative analysis table from Area 2. Only 30% of the material analyzed appears to preserve the low crystallinity of pyrogenic calcite.

Density Separation and SEM-CL

The KW mortars contain a large number of lime lumps, which are composed of a mixture of Ca(OH)_2 and CaCO_3 . These components pose two major contamination problems. First, the CaCO_3 fraction that they contain might have carbonated well after the mortar was set in place. Second, residual Ca(OH)_2 can react with present-day CO_2 once it is exposed during sample preparation. Therefore, we avoided macroscopic lime lumps and we checked with FTIR the occurrence of the Ca(OH)_2 peak at 3644 cm^{-1} in the powders selected for density separation. In three cases, KW4213A-B and KW4215A, we purified powders containing Ca(OH)_2 . This phase dissolves in SPT, but it may carbonate during crushing and sieving of the sample. For other measurements, KW4213C and KW4215B-C, we purified only

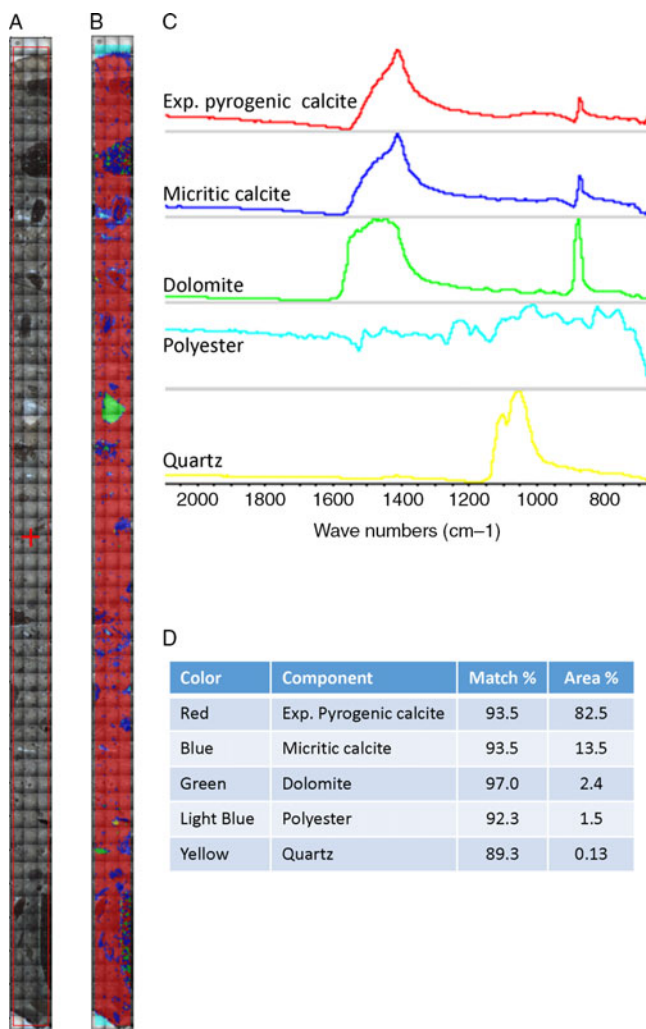


Figure 7 Micro-FTIR chemical map of KW4213 showing areas characterized by different phases. A: video mosaic mapped reflection mode. B: color-coded chemical map. C: reference FTIR spectra used to create the chemical map. D: quantitative analysis table. Note that over 80% of the area analyzed appears to be composed of calcite with FTIR spectral characteristics similar to those of experimental pyrogenic calcite (i.e. experimental lime plaster).

powders devoid of $\text{Ca}(\text{OH})_2$, to the best of FTIR accuracy ($\sim 1\%$). The efficiency of density separation at 2.5 g/mL was 15% for SHV and 75–80% for KW. In case of low yield as for SHV, we repeated the procedure other three times, for a total of 3.2 g of starting material (as opposed to 800 mg for each KW mortar). As a general rule of thumb, we advise recovering at least 400 mg of light fraction to obtain larger CO_2 yields during thermal decomposition. LDHs and ettringite have low specific gravities (< 2.2 g/mL) and thus are always confined to the light fraction. For this reason, the KW mortars show much higher efficiency compared to SHV, which contains only calcite. In order to reduce the rounds of density separation when there is less than 15% supernatant left, the density of the

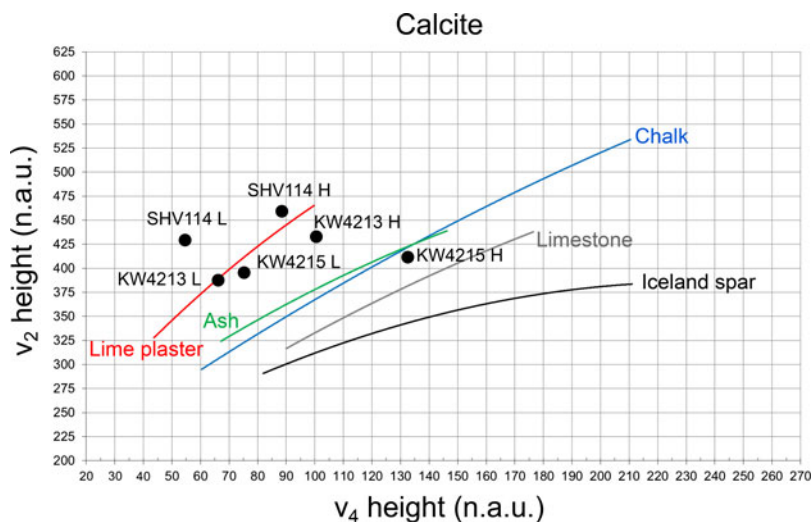


Figure 8 FTIR grinding curve plot of calcite showing trend lines for standard reference materials and points for archaeological samples after density separation (n.a.u.: normalized absorbance units; L: light fraction; H: heavy fraction). Well-preserved fractions cluster around the trend line of experimental lime plaster.

SPT/buffer mixture may be increased based on the nature of the material, but should never be higher than 2.6 g/mL to avoid large amounts of geogenic contaminants (the specific gravity of calcite is 2.71 g/mL). Light and heavy fractions were analyzed with FTIR to assess their degree of purity. Results show that supernatants are poorly ordered, similar to experimental plaster, whereas heavy fractions are relatively well ordered (Figure 8).

Supernatants were analyzed with SEM-CL to verify the presence of geogenic carbonate contaminants, which emit light of different color compared to the pyrogenic binder. As shown in Figure 9, the SHV and KW point analyses are characterized by two major emissions. One occurs in the blue at 450 nm for SHV and 455 nm for KW, whereas the second is centered around 600 nm in the orange for both samples and includes a shoulder at 560 nm (yellow). Considering that we avoided areas with silicates or metal oxides based on energy dispersive spectroscopy maps of the pellets, we can correlate these emissions with different types of carbonates. The 600 nm band is caused by residual geogenic calcite and dolomite, which are known to emit in the orange-red due to the presence of Mn^{2+} activators (Götze 2012). Alternatively, the orange emission may be attributed to recrystallized calcite that incorporated Mn^{2+} from the environment (e.g. Wassenburg et al. 2012). The 450 nm band is instead related to pyrogenic calcite. Previous studies exclusively based on color described the preserved binder as “tile red”, “brown”, “dark red” and “dull purple” (Heinemeier et al. 1997; Lindroos et al. 2007; Heinemeier et al. 2010; Murakami et al. 2013). While of difficult interpretation based on subjective observation of samples through a microscope eyepiece or in photo, these hues may be considered as the combined contribution of a red component caused by Mn^{2+} activators that substitute for Ca^{2+} in the calcite crystal lattice, and of one or more blue components related to the intrinsic centers that promote blue luminescence in calcite (Habermann et al. 2000). The cause of this blue emission in plaster is currently unknown, although it was recently shown that it is related to the breakdown of carbonate groups during thermal decomposition of $CaCO_3$ (including

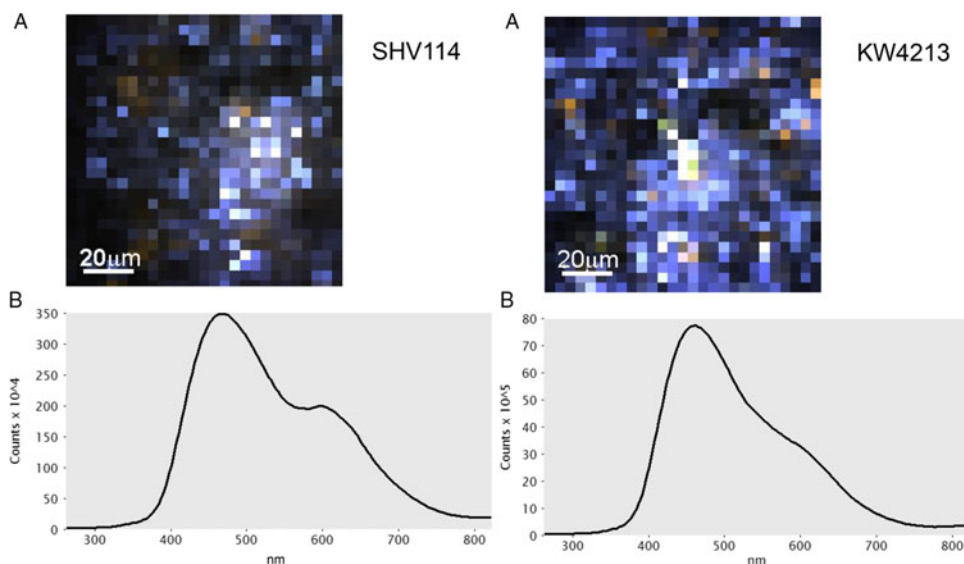


Figure 9 SEM-CL spectra of SHV114 and KW4213. A: colored spectrum imaging map. Each pixel corresponds to a CL measurement over an area of $4.3 \times 4.3 \mu\text{m}$. B: CL spectrum.

MnCO₃ sites) to obtain quicklime, which promotes the displacement of Mn²⁺ present in limestone and dolomite (Kusano et al. 2014; Toffolo et al. 2019b). In addition, in the high Eh and pH environment of Ca(OH)₂, Mn precipitates preferentially in the form of oxide and hydroxide (Machel 2000). Interestingly, most of the measurements for both samples show that the 450 nm band is dominant or occurs alone, indicating that most of the material is pyrogenic. However, the few orange bands lend support to the hypothesis put forward by Toffolo et al. (2017a) that residual geogenic or recrystallized components containing Mn²⁺ occur as well. Therefore, it is possible to note a correlation between FTIR and SEM-CL in terms of local structural order of calcite crystals, with poorly ordered calcite consistently emitting blue luminescence (Toffolo et al. 2019b). The information gathered with SEM-CL could be potentially used to quantify the degree of preservation of the lime binder.

Thermal Decomposition and Radiocarbon Dating

Results of TGA in nitrogen atmosphere show that the SHV light fraction starts decomposing at 500°C, whereas the major weight loss occurs between 650 and 750°C (Figure 10). Considering that this is the light fraction and crystals are poorly ordered, we still do not understand the reason for such an elevated decomposition temperature. The KW light fractions appear to be more complex due to the presence of LDH phases, which decompose at temperatures below 500°C. In particular, the peak at ~110°C may be associated with ettringite, whereas the peaks at 190–200, 360–380 and 470°C represent the decomposition steps of phases such as hydrotalcite, hydrocalumite, brucite and pyroaurite-2H. Calcite starts decomposing at 450–500°C, and a notable shoulder at 620–630°C may represent secondary calcite observed in thin section. Similar to SHV, the major weight loss occurs between 650 and 750°C. When the sample is heated for 1 hr at 500°C, a small amount of CO₂ is released. Therefore, for CO₂ recovery we set temperature steps at 500°C for both samples, and for KW4213B we collected CO₂ from a step at 550°C.

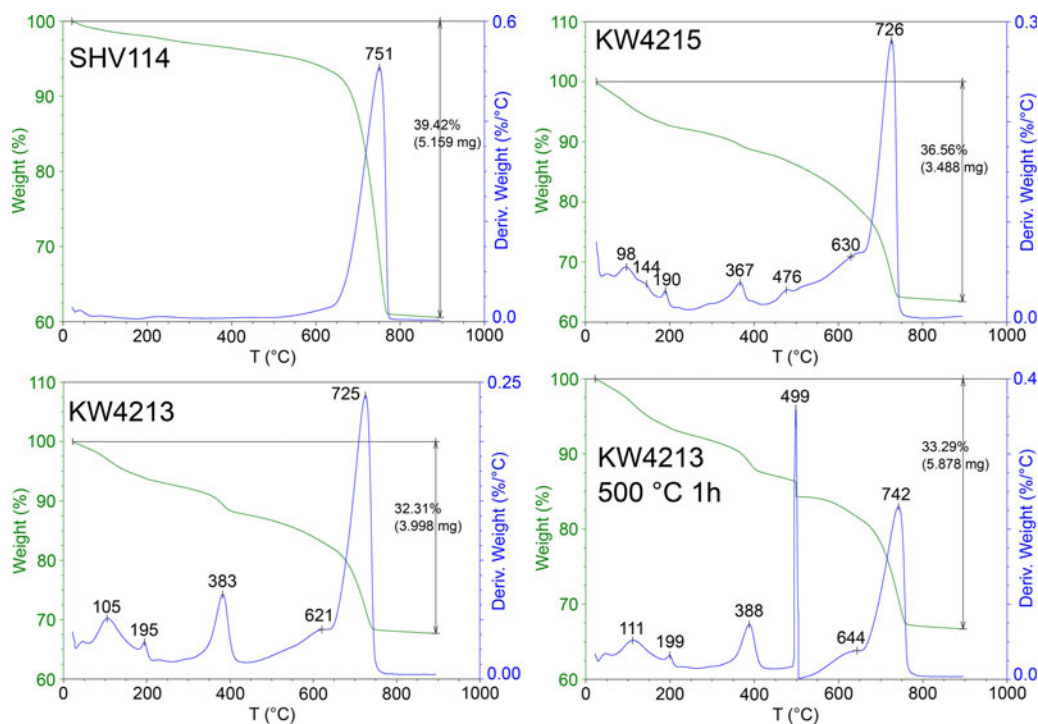


Figure 10 TGA plots of SHV114, KW4213 and KW4215, including a 500°C heating step of 1 hr for KW4213. The latter shows that a small amount of CO₂ is released.

Results of thermal decomposition and ¹⁴C measurements are displayed in Table 2. Light fractions were initially heated to 500°C, a temperature that released a small amount of CO₂. The second temperature step at 700°C produced a larger quantity of CO₂, due to the decomposition of more ordered, recrystallized and residual geogenic calcite (Toffolo et al. 2017a). This is confirmed by the lower pMC observed at higher temperature. In the case of SHV114A, the 500°C aliquot of the light fraction matches the expected pMC range of the Byzantine church, whereas the 700°C aliquot yielded lower pMC. All the temperature aliquots of the heavy fraction are affected by dead carbon. SHV114B at 500°C produced an age younger by 1.6 pMC compared to SHV114A, at the transition between Byzantine and Early Islamic periods (7th c. CE). SHV114C is statistically in agreement with SHV114B, as the standard deviations of the two samples overlap. Measurements appear to be reproducible, although the pMC variation between SHV114A and SHV114B-C requires further understanding.

KW mortars follow the same trend, with pMC decreasing at increasing temperature. The light fraction of KW4213A at 500°C is younger by 1.1 pMC compared to the reference cellulose from embedded linen/straw. The calibrated ranges overlap at the 2σ range, but do not pass the χ² test. Light fractions of KW4213B (550°C), KW4215A, KW4215B and KW4215C (500°C) show slightly higher pMC compared to the reference cellulose. All of these offsets are likely caused by the presence of lime lumps that carbonated at a later stage or during sample preparation. Only the light fraction of KW4213C shows a lower pMC compared to the reference. This can only be explained by the presence of geogenic residues that density

Table 2 ^{14}C dating results showing laboratory number, material, size and pMC. Letters (A, B, C) mark different aliquots of a specific sample.

| Lab nr | Material | Size (mg of carbon) | pMC | ^{14}C age $\pm 1\sigma$ BP | Matches expected age |
|---------|---|---------------------------|----------------|---|----------------------------|
| RTD9048 | SHV114A Plaster <50 μm <2.5 g/mL, 500°C | 0.14 | 82.7 \pm 0.3 | 1524 \pm 30 | Yes |
| RTD9048 | SHV114A Plaster <50 μm <2.5 g/mL, 700°C | 0.59 | 66.6 \pm 0.2 | 3256 \pm 27 | No |
| RTD9048 | SHV114A Plaster <50 μm >2.5 g/mL, 500°C | 0.11 | 79.9 \pm 0.4 | 1796 \pm 45 | No |
| RTD9048 | SHV114A Plaster <50 μm >2.5 g/mL, 700°C | 0.84 | 68.9 \pm 0.2 | 2984 \pm 26 | No |
| RTD9048 | SHV114A Plaster <50 μm >2.5 g/mL, 800°C | 1.02 | 37.1 \pm 0.2 | 7944 \pm 53 | No |
| RTD9698 | SHV114B Plaster not sieved <2.5 g/mL, 500°C | 0.28 | 84.3 \pm 0.2 | 1366 \pm 26 | No |
| RTD9990 | SHV114C Plaster <63 μm <2.5 g/mL, 500°C | 0.18 | 84.7 \pm 0.2 | 1328 \pm 26 | No |
| RTD9417 | KW4213A Mortar <63 μm <2.5 g/mL, 500°C | 0.21 | 94.2 \pm 0.3 | 478 \pm 32 | ? |
| RTD9417 | KW4213A Mortar <63 μm <2.5 g/mL, 700°C | 1.02 | 86.3 \pm 0.3 | 1181 \pm 34 | No |
| RTD9695 | KW4213B Mortar <63 μm <2.5 g/mL, 550°C | 0.58 | 95.1 \pm 0.2 | 398 \pm 18 | No |
| RTD9987 | KW4213C Mortar <50 μm <2.5 g/mL, 500°C | 0.09 | 90.0 \pm 1.1 | 843 \pm 103 | No |
| RTD9014 | KW4213 grass cellulose | 1.02 | 93.0 \pm 0.4 | 577 \pm 35 | — |
| RTD9696 | KW4215A Mortar <63 μm <2.5 g/mL, 500°C | 0.66 | 95.4 \pm 0.2 | 370 \pm 21 | No |
| RTD9696 | KW4215A Mortar <63 μm <2.5 g/mL, 700°C | 1.05 | 92.9 \pm 0.3 | 588 \pm 31 | Yes |
| RTD9988 | KW4215B Mortar <50 μm <2.5 g/mL, 500°C | 0.18 | 94.8 \pm 0.3 | 428 \pm 30 | No |
| RTD9989 | KW4215C Mortar <50 μm <2.5 g/mL, 500°C | 0.16 | 95.1 \pm 0.3 | 402 \pm 27 | No |
| RTD9016 | KW4215 grass cellulose | 1.00 | 93.2 \pm 0.3 | 558 \pm 33 | — |
| RTD9638 | KW4215 grass cellulose | 1.04 | 92.9 \pm 0.1 | 585 \pm 12 | — |

separation could not remove. It thus seems that thermal decomposition can remove LDHs, but the presence of lime lumps that carbonate during sample preparation hinders accurate dating of the KW mortars.

Implementation of the Method

The approach to mortar dating presented in this study aims at providing accurate age determinations based on the identification of a pristine pyrogenic fraction *prior* to CO_2 recovery. Sample characterization and density separation are meant to overcome the contribution of carbonate contaminants from aggregates and secondary phases that in the

past hampered the application of the thermal decomposition method proposed by Labeyrie and Delibrias (1964).

Analyses using methods that address short- and long-range atomic order in crystals (FTIR and XRD, respectively) provide a first screening of materials that are suitable for dating. In particular, with FTIR it is possible to assess the degree of preservation of CaCO₃ crystals based on intensity and broadening of their infrared absorptions, and thus immediately discard samples that show evidence of extensive recrystallization of the pyrogenic binder as compared to experimental lime plaster standards (Regev et al. 2010; Toffolo et al. 2019a). For instance, extremely old materials embedded in sediments exposed to groundwater are more likely to have lost their original isotopic composition due to recrystallization, as is the case of several Pre-Pottery Neolithic lime plaster floors from Yiftahel in Israel (Poduska et al. 2012). It follows that some materials cannot be dated with accuracy. XRD determines the presence of other carbonate-bearing secondary phases, such as LDH, that need to be taken into account during thermal decomposition. Due to their relatively ease of use and short turnaround time, FTIR and XRD characterization of a number of samples may be performed rather quickly. If samples are suitable for dating, thin sections should be prepared to observe the spatial distribution of different components and the extent of recrystallization or nucleation of secondary phases (e.g. only at the surface, concentrated in pores, extensive throughout the sample). Furthermore, μ FTIR may provide important insights into the location of preserved CaCO₃ crystals compared to bulk FTIR using homogenized KBr pellets, and the locales rich in portlandite. This information may be used in the future prior to carbon recovery via laser ablation (e.g. Yeman et al., 2020).

In order to remove geogenic contaminants and part of the secondary phases, powdered samples are treated with buffered SPT. Depending on the size of centrifuges at disposal, the extraction of light carbonates from 800 mg of starting material requires 1 hr. The advantage of this procedure is the possibility of obtaining purified fractions larger than 500 mg in a relatively short time. Such amounts are important for CO₂ recovery, as generally thermal decomposition at 500°C yields less than 1 mg of carbon. The purity of light carbonates is verified using FTIR and the grinding curve method. However, some contaminants may still occur (Toffolo et al. 2017a). In this study, this has been shown using SEM-CL, based on the different luminescence wavelengths of geogenic and pyrogenic calcite. To recover CO₂ only from poorly ordered, pyrogenic calcite and thus avoid contribution from residual contaminants and especially LDH in hydraulic mortars (e.g. Addis et al. 2019), thermal decomposition was privileged over acid hydrolysis. The latter requires acid to come in contact with all particles, a process that is not homogeneous throughout the sample at any given time due to the presence of intergrown pyrogenic-geogenic aggregates that may dissolve at the same time. Moreover, if LDHs are present, they will dissolve together with pyrogenic calcite due to their similar solubility. Heat instead affects homogeneously all particles at the same time at the same temperature. By knowing the thermal behavior of the sample using TGA and its mineral composition, it is possible to predict to a certain extent which phases will decompose at any given temperature. With acid hydrolysis, contamination may be detected only based on ¹⁴C measurements (Heinemeier et al. 2010).

The abovementioned approach provided accurate ages for the SHV plaster. The difference in pMC between SHV114 A and B must be sought in the relatively high amount of well-ordered calcite in the purified fraction, represented by a peak at ~750°C in the TGA plot (Figure 10). This could be a result of the use of different sieve meshes between SHV114A (50 μ m) and

SHV114C (63 μm), with the larger one allowing the collection of coarser grains of possible geologic origin. In addition, SHV114B was not sieved and thus may have contained more geogenic calcite. In the case of the KW mortars, TGA results suggest that LDHs decompose below 500°C, and thus the younger ages obtained are probably caused by the presence of unknown amounts of $\text{Ca}(\text{OH})_2$ in the starting material. Future research will address this point by treating mortars in a controlled carbon-free atmosphere.

CONCLUSIONS

Accurate ^{14}C dating of mortars is a challenging task that requires a multi-disciplinary approach. Results reported herein show that it is possible to obtain accurate ages from aerial lime mortars using the thermal decomposition method, and that hydraulic mortars may be accurately dated if lime lumps are absent. To succeed in such an endeavor, it is of the utmost importance to thoroughly characterize the sample and understand its behavior when exposed to the elevated temperatures necessary for CO_2 recovery. Obviously, this should be carried out *before* ^{14}C measurements. Different samples have different composition, even within the same architectural feature, and therefore require a dedicated strategy in terms of decomposition temperature. Nevertheless, we have proposed here a general procedure that may be applied to a wide range of aerial binders to target pyrogenic calcite or aragonite. A first stage of “bulk” characterization including FTIR and XRD aims at the identification of contaminants such as geogenic and diagenetic calcite, and LDH phases. A second stage of detailed “spatial” characterization combines bulk data with the observation and analysis of thin sections using petrographic and FTIR microscopes. Once the pyrogenic fraction has been characterized, it is isolated by density and its purity is verified again using FTIR. In the future, SEM-CL may be used to quantify the degree of atomic order of calcite in the purified fraction. Finally, TGA provides temperature steps for CO_2 recovery, and thus allows avoiding residual contaminants that decompose at lower and higher temperatures compared to the pyrogenic fraction. The main requirement of this approach is that the lime binder is not affected by extensive carbon mixing caused by diagenetic recrystallization of CaCO_3 crystals, as is usually the case for prehistoric materials or more recent materials deposited in unfavorable sedimentary contexts. In our experience, based on the analysis of several archaeological plasters and mortars using FTIR, materials within standing structures from the last ~3000 years are likely to preserve their original isotopic signature and thus may produce accurate age determinations.

ACKNOWLEDGMENTS

This research was supported by a grant from IdEx Bordeaux to Michael Toffolo (grant n. ANR-10-IDEX-03-02), and by the Exilarch’s Foundation for the Dangoor Research Accelerator Mass Spectrometer (D-REAMS). Elisabetta Boaretto is the incumbent of the Dangoor Professorial Chair of Archaeological Sciences. The authors wish to thank Joe Uziel for providing mortar samples from Wilson’s Arch, Guy Bar-Oz and Yotam Tepper for providing the plaster sample from Shivta, and Brigitte Spiteri for preparing thin sections at the IRAMAT-CRP2A.

SUPPLEMENTARY MATERIAL

To view supplementary material for this article, please visit <https://doi.org/10.1017/RDC.2020.39>

REFERENCES

- Addis A, Secco M, Preto N, Marzaioli F, Passariello I, Brogiolo GP, Chavarria Arnau A, Artioli G, Terrasi F. 2016. New strategies for radiocarbon dating of mortars: Multi-step purification of the lime binder. In: Papayianni I, Stefanidou M, Pachta V, editors. Proceedings of the 4th Historic Mortar Conference, 10–12 October 2016, Santorini. p. 665–672.
- Addis A, Secco M, Marzaioli F, Artioli G, Chavarria Arnau A, Passariello I, Terrasi F, Brogiolo GP. 2019. Selecting the most reliable ^{14}C dating material inside mortars: the origin of the Padua Cathedral. *Radiocarbon* 61(2):375–393.
- Anastasiou M, Hasapis T, Zorba T, Pavlidou E, Chrissafis K, Paraskevopoulos KM. 2006. TG-DTA and FTIR analyses of plasters from Byzantine monuments in Balkan region. *Journal of Thermal Analysis and Calorimetry* 84(1): 27–32.
- Artioli G. 2010. Scientific methods and cultural heritage: An introduction to the application of materials science to archaeometry and conservation science. Oxford: Oxford University Press.
- Artioli G, Secco M, Addis A, Bellotto M. 2017. Role of hydrotalcite-type layered double hydroxides in delayed pozzolanic reactions and their bearing on mortar dating. In: Pöllmann H, editor. *Cementitious materials: Composition, properties, application*. Berlin: De Gruyter. p. 147–158.
- Avni G. 2014. The Byzantine-Islamic transition in Palestine: an archaeological approach. Oxford: Oxford University Press.
- Baxter MS, Walton A. 1970. Radiocarbon dating of mortars. *Nature* 225:937–938.
- Berna F, Goldberg P, Kolska Horwitz L, Brink J, Holt S, Bamford M, Chazan M. 2012. Microstratigraphic evidence of in situ fire in the Acheulean strata of Wonderwerk Cave, Northern Cape province, South Africa. *PNAS* 109:E1215–E20.
- Boaretto E, Poduska KM. 2013. Materials science challenges in radiocarbon dating: The Case of archaeological plasters. *Journal of the Minerals, Metals & Materials Society (TMS)* 65:481–488.
- Boynton RS. 1980. *Chemistry and technology of lime and limestone*. New York: John Wiley & Sons, Inc.
- Delibrias G, Labeyrie J. 1965. The dating of mortars by the carbon-14 method. In: Chatters RM, Olson EA, editors. Proceedings of the 6th International Conference on Radiocarbon and Tritium Dating, 7–11 June 1965, Pullman, WA. p 344–347.
- Farmer VC. 1974. The infrared spectra of minerals. London: Mineralogical Society.
- Folk RL, Valastro S. 1976. Successful technique for dating of lime mortar by carbon-14. *Journal of Field Archaeology* 3(2):203–208.
- Götze J. 2012. Application of cathodoluminescence microscopy and spectroscopy in geosciences. *Microscopy and Microanalysis* 18:1270–1284.
- Habermann D, Neuser RD, Richter DK. 2000. Quantitative high resolution analysis of Mn^{2+} in sedimentary calcite. In: Pagel M, Barbin V, Blanc P, Ohnenstetter D, editors. *Cathodoluminescence in Geosciences*. Berlin: Springer Verlag. p. 331–358.
- Hajdas I, Lindroos A, Heinemeier J, Ringbom Å, Marzaioli F, Terrasi F, Passariello I, Capano M, Artioli G, Addis A, Secco M, Michalska D, Czernik J, Goslar T, Hayen R, Van Strydonck M, Fontaine L, Boudin M, Maspero F, Panzeri L, Galli A, Urbanova P, Guibert P. 2017. Preparation and dating of mortar samples-Mortar Dating Intercomparison Study (MODIS). *Radiocarbon* 59(5):1–14.
- Hayen R, Van Strydonck M, Fontaine L, Boudin M, Lindroos A, Heinemeier J, Ringbom Å, Michalska D, Hajdas I, Hueglin S, Marzaioli F, Terrasi F, Passariello I, Capano M, Maspero F, Panzeri L, Galli A, Artioli G, Addis A, Secco M, Boaretto E, Moreau C, Guibert P, Urbanova P, Czernik J, Goslar T, Caroselli M. 2017. Mortar dating methodology: Assessing recurrent issues and needs for future research. *Radiocarbon* 59(6):1859–1871.
- Heinemeier J, Jungner H, Lindroos A, Ringbom Å, von Konow T, Rud N. 1997. AMS ^{14}C dating of lime mortar. *Nuclear Instruments and Methods in Physics Research Section B: Beam Interactions with Materials and Atoms* 123:487–495.
- Heinemeier J, Ringbom Å, Lindroos A, Sveinbjörndóttir Á. 2010. Successful AMS ^{14}C dating of non-hydraulic lime mortars from the medieval churches of the Åland Islands, Finland. *Radiocarbon* 52(1):171–204.
- Ishihara S, Sahoo P, Deguchi K, Ohki S, Tansho M, Shimizu T, Labuta J, Hill JP, Ariga K, Watanabe K, Yamauchi Y, Suehara S, Iyi N. 2013. Dynamic breathing of CO_2 by hydrotalcite. *Journal of the American Chemical Society* 135:18040–18043.
- Karkanas P. 2007. Identification of lime plaster in prehistory using petrographic methods: a review and reconsideration of the data on the basis of experimental and case studies. *Geoarchaeology* 22:775–796.
- Kingery WD, Vandiver PB, Prickett M. 1988. The beginnings of pyrotechnology. Part II: Production and use of lime and gypsum plaster in the pre-pottery Neolithic Near East. *Journal of Field Archaeology* 15(2):219–244.
- Koumouzelis M, Ginter B, Kozłowski JK, Pawlikowski M, Bar-Yosef O, Albert RM, Litynska-Zajac M, Storzewicz E, Wojtal P, Lipecki G, Tomek T, Bochenski ZM, Pazdur A. 2001. The early Upper Palaeolithic in Greece: the excavations in Klisoura Cave. *Journal of Archaeological Science* 28:515–539.
- Kusano N, Nishido H, Inoue K. 2014. Cathodoluminescence of calcite decomposed

- from dolomite in high-temperature skarn. *Journal of Mineralogical and Petrological Sciences* 109: 286–290.
- Labeyrie J, Delibrias G. 1964. Dating of old mortars by the carbon-14 method. *Nature* 201:742.
- Lindroos A, Heinemeier J, Ringbom Å, Braskén M, Sveinbjörndóttir Á. 2007. Mortar dating using AMS ^{14}C and sequential dissolution: examples from medieval, non-hydraulic lime mortars from the Åland Islands, SW Finland. *Radiocarbon* 49:47–67.
- Lippmann F. 1973. *Sedimentary carbonate minerals*. Heidelberg: Springer.
- Machel HG. 2000. Application of cathodoluminescence to carbonate diagenesis. In: Pagel M, Barbin V, Blanc P, Ohnenstetter D, editors. *Cathodoluminescence in geosciences*. Berlin: Springer Verlag. p. 271–301.
- Michalska D. 2019. Influence of different pre-treatments on mortar dating results. *Nuclear Instruments and Methods in Physics Research Section B: Beam Interactions with Materials and Atoms* 456:236–246.
- Mills SJ, Christy AG, Génin J-MR, Kameda T, Colombo F. 2012. Nomenclature of the hydrotalcite supergroup: natural layered double hydroxides. *Mineralogical Magazine* 76(5): 1289–1336.
- Moropoulou A, Bakolas A, Bisbikou K. 1995. Characterization of ancient, byzantine and later historic mortars by thermal and X-ray diffraction techniques. *Thermochimica Acta* 269/270: 779–795.
- Murakami T, Hodgins G, Simon AW. 2013. Characterization of lime carbonates in plasters from Teotihuacan, Mexico: Preliminary results of cathodoluminescence and carbon isotope analyses. *Journal of Archaeological Science* 40: 960–970.
- Poduska KM, Regev L, Boaretto E, Addadi L, Weiner S, Kronik L, Curtarolo S. 2011. Decoupling local disorder and optical effects in infrared spectra: Differentiating between calcites with different origins. *Advanced Materials* 23: 550–554.
- Poduska KM, Regev L, Berna F, Mintz E, Milevski I, Khalaily H, Weiner S, Boaretto E. 2012. Plaster characterization at the PPNB site of Yiftahel (Israel) including the use of ^{14}C : implications for plaster production, preservation, and dating. *Radiocarbon* 54:887–896.
- Pöllmann H. 2017. *Cementitious materials: Composition, properties, application*. Berlin: De Gruyter.
- Ponce-Antón G, Ortega LA, Zuluaga MC, Alonso-Olazabal A, Solaun JL. 2018. Hydrotalcite and hydrocalumite in mortar binders from the medieval Castle of Portilla (Álava, North Spain): Accurate mineralogical control to achieve more reliable chronological ages. *Minerals* 8:326.
- Regev L, Poduska KM, Addadi L, Weiner S, Boaretto E. 2010. Distinguishing between calcites formed by different mechanisms using infrared spectrometry: archaeological applications. *Journal of Archaeological Science* 37(12): 3022–3029.
- Regev L, Eckmeier E, Mintz E, Weiner S, Boaretto E. 2011. Radiocarbon concentrations of wood ash calcite: Potential for dating. *Radiocarbon* 53(1):117–127.
- Regev L, Steier P, Shachar Y, Mintz E, Wild EM, Kutschera W, Boaretto E. 2017. D-REAMS: A new compact AMS system for radiocarbon measurements at the Weizmann Institute of Science, Rehovot, Israel. *Radiocarbon* 59: 775–784.
- Rey F, Fornés V, Rojo JM. 1992. Thermal decomposition of hydrotalcites: An infrared and nuclear magnetic resonance spectroscopic study. *Journal of the Chemical Society, Faraday Transactions* 88(15):2233–2238.
- Ringbom Å, Lindroos A, Heinemeier J, Sonck-Koota P. 2014. 19 years of mortar dating: Learning from experience. *Radiocarbon* 56:619–635.
- Roelofs JCAA, van Bokhoven JA, van Dillen AJ, Geus JW, de Jong KP. 2002. The thermal decomposition of Mg-Al hydrotalcites: Effects of interlayer anions and characteristics of the final structure. *Chemistry: A European Journal* 8(24):5571–5579.
- Sahoo P, Ishihara S, Yamada K, Deguchi K, Ohki S, Tansho M, Shimizu T, Eisaku N, Sasai R, Labuta J, Ishikawa D, Hill JP, Ariga K, Bastakoti BP, Yamauchi Y, Iyi N. 2014. Rapid exchange between atmospheric CO_2 and carbonate anion intercalated within magnesium rich layered double hydroxide. *Applied Materials and Interfaces* 6:18352–18359.
- Stuiver M, Smith CS. 1965. Radiocarbon dating of ancient mortar and plaster. In: Chatters RM, Olson EA, editors. *Proceedings of the 6th International Conference on Radiocarbon and Tritium Dating, 7–11 June 1965, Pullman, WA*. p. 338–343.
- Tepper Y, Erickson-Gini T, Farhi Y, Bar-Oz G. 2018. Probing the Byzantine/Early Islamic transition in the Negev: The renewed Shivta excavations, 2015–2016. *Tel Aviv* 45(1):120–152.
- Tian J, Qinghai G. 2014. Thermal decomposition of hydrocalumite over a temperature range of 400–1500°C and its structure reconstruction in water. *Journal of Chemistry* 2014:454098.
- Toffolo MB, Boaretto E. 2014. Nucleation of aragonite upon carbonation of calcium oxide and calcium hydroxide at ambient temperatures and pressures: a new indicator of fire-related human activities. *Journal of Archaeological Science* 49:237–248.
- Toffolo MB, Regev L, Mintz E, Poduska KM, Shahack-Gross R, Berthold C, Miller CE, Boaretto E. 2017a. Accurate radiocarbon dating

- of archaeological ash using pyrogenic aragonite. *Radiocarbon* 59:231–249.
- Toffolo MB, Ullman M, Caracuta V, Weiner S, Boaretto E. 2017b. A 10,400-year-old sunken lime kiln from the Early Pre-Pottery Neolithic B at the Neshar-RamLa quarry (el-Khirbe), Israel. *Journal of Archaeological Science: Reports* 14:353–364.
- Toffolo MB, Regev L, Dubernet S, Lefrais Y, Boaretto E. 2019a. FTIR-based crystallinity assessment of aragonite–calcite mixtures in archaeological lime binders altered by diagenesis. *Minerals* 9(2):121.
- Toffolo MB, Ricci G, Caneve L, Kaplan-Ashiri I. 2019b. Luminescence reveals variations in local structural order of calcium carbonate polymorphs formed by different mechanisms. *Scientific Reports* 9:16170.
- Uziel J, Lieberman T, Solomon A. 2019. The best show in town: The excavations beneath Wilson’s Arch and their importance in understanding Jerusalem in the early and late Roman periods. *Tel Aviv* 46(2).
- van der Marel HW, Beutelspacher H. 1976. *Atlas of infrared spectroscopy of clay minerals and their admixtures*. Amsterdam: Elsevier Scientific Publishing Company.
- Wassenburg JA, Immenhauser A, Richter DK, Jochum KP, Fietzke J, Deininger M, Goos M, Scholz D, Sabaoui A. 2012. Climate and cave control on Pleistocene/Holocene calcite-to-aragonite transitions in speleothems from Morocco: Elemental and isotopic evidence. *Geochimica et Cosmochimica Acta* 92:23–47.
- Weiner S. 2010. *Microarchaeology. Beyond the visible archaeological record*. New York: Cambridge University Press.
- Xu B, Toffolo MB, Regev L, Boaretto E, Poduska KM. 2015. Structural differences in archaeologically relevant calcite. *Analytical Methods* 7:9304–9309.
- Xu B, Toffolo MB, Boaretto E, Poduska KM. 2016. Assessing local and long-range structural disorder in aggregate-free lime binders. *Industrial & Engineering Chemistry Research* 55: 8334–8340.
- Yeman C, Christl M, Hattendorf B, Wacker L, Welte C, Brehm N, Synal H-A. 2020. Unravelling quasi-continuous ¹⁴C profiles by laser ablation AMS. *Radiocarbon* 62(2):453–465.
- Yizhaq M, Mintz G, Cohen I, Khalaily H, Weiner S, Boaretto E. 2005. Quality controlled radiocarbon dating of bones and charcoal from the early Pre-Pottery Neolithic B (PPNB) of Motza (Israel). *Radiocarbon* 47(2):193–206.
- Zouridakis N, Saliege JF, Person A, Filippakis SE. 1987. Radiocarbon dating of mortars from ancient Greek palaces. *Archaeometry* 29(1):60–8.